Journal of Molecular Catalysis A: Chemical 324 (2010) 133–140

Contents lists available at ScienceDirect

Journal of Molecular Catalysis A: Chemical

journal homepage: www.elsevier.com/locate/molcata

Computational catalysis

A systematic study on the RuHCl–BINAP-catalyzed asymmetric hydrogenation mechanism by the global reaction route mapping method☆

Koichi Ohno*, Satoshi Maeda

Department of Chemistry, Graduate School of Science, Tohoku University, Aramaki, Aoba-ku, Sendai 980-8578, Japan

ARTICLE INFO

Article history:
Available online 6 March 2010

Keywords:
Asymmetric hydrogenation
Transition state structure
Chirality determining step, Automated exploration

ABSTRACT

Anharmonic downward distortion (ADD) of potential energy surfaces (PES) indicates the direction of reaction routes, and the ADD-following on PES has made it possible to perform global reaction route mapping (GRRM) of a given chemical formula. The GRRM method based on the ADD-following can be applied to real processes of catalytic reactions to elucidate the reaction mechanisms. A systematic analysis of a RuHCl–BINAP-catalyzed asymmetric hydrogenation reaction has given an insight into the role of important adsorption structures and the chirality determining transition state among numerous candidates. Computed reaction profiles for the total catalytic cycles with and without protonation demonstrated significance of the protonation for both high enantioselectivity and high catalytic-activity.

1. Introduction

Asymmetric hydrogenation is very powerful for producing enantioenriched compounds without forming any wastes [1–3]. Asymmetric hydrogenation uses a chiral molecular catalyst which is designed to enhance both enantioselectivity and catalytic-activity. Various chiral catalysts have been synthesized and employed in industry [4], and further developments are undergoing very actively. The selectivity is controlled at a transition state (TS) structure of the chirality determining reaction step: the high selectivity is achieved by designing the TS structure connected to the useful enantiomer as low as possible in energy compared to that for the useless one. On the other hand, the catalytic-activity changes depending on a choice of the metallic elements, anionic ligands, and so on. These two factors determine the efficiency of asymmetric hydrogenation. It was suggested that a deep insight into mechanisms is indispensable for developing a truly efficient asymmetric hydrogenation [5].

To elucidate reaction mechanisms involving homogeneous organometallic catalysts, theoretical calculations have become a powerful tool because of recent advances in computers and computation techniques [6–11]. Development of various approaches in the density functional theory (DFT) [12,13], the new semi-empirical methods [14,15], the molecular mechanics (MM) methods [16], and the QM/MM [17–19] and the more general ONIOM [20–22] methods considerably improved applicability and reliability of theoretical calculations to complex organometallic catalytic reactions. Development of efficient geometry optimization techniques [23] is also very important. In these years, optimizations of TS structures are routinely done for small model systems. Geometry optimization studies have been performed also for asymmetric hydrogenation reactions, and the experimental selectivity has been explained successfully [24–27]. Although such geometry optimization studies have considered only a few TS structures for each elementary-step, there are numerous TS structures even for only one elementary-step of an asymmetric hydrogenation reaction, because of the complexity of its potential energy surface (PES). The complexity is due to the introduction of bulky ligands in the asymmetric catalysts for high selectivity. Hence, a systematic exploration of PES [28] is necessary for obtaining the lowest TS structure which determines the selectivity.

Recently, the authors [29] and Donoghue et al. [30] performed such systematic analyses individually by using different theoretical approaches. Donoghue et al. employed the QM-guided molecular mechanics (Q2MM) force-field [16], which was parameterized specially for Rh-catalyzed hydrogenation [31] in Monte-Carlo simulations. They performed calculations on extensive test systems including 11 chiral phosphino-ligands and 7 reactant/product molecules, and demonstrated the successful rapid screening of chiral catalysts *in silico* for the hydrogenation of enamides. On the other hand, the authors explored PES of the ONIOM method [20–22] by the global reaction route mapping (GRRM) method [32–34]. Although only one system was studied, as many as 68 TS structures could be located for a single chirality determining elementary-step in the QM/MM-ONIOM framework, which excel-

☆ This paper is part of a special issue on Computational Catalysis.

* Corresponding author. Present address: Toyota Physical and Chemical Research Institute, Nagakute, Aichi 480-1192, Japan.
E-mail addresses: ohnok@mail.tains.tohoku.ac.jp, ohnok@gakushikai.jp (K. Ohno).

1381-1169/$ – see front matter © 2010 Elsevier B.V. All rights reserved.
doi:10.1016/j.molcata.2010.03.004

lently reproduced the experimental enantio-excess (%ee) value. Mechanistic reasons of the selectivity could be explained based on the accurate TS structures for the future catalyst design. One advantage of the ONIOM–GRRM approach is that applications to different systems are straightforward, since no system-specific reparameterization is required. This is especially important in studies on the catalytic-activity, because replacements of metallic elements, anionic ligands, and so on can change electronic structures as well as reactivity significantly.

Here, the GRRM method has made it possible to perform an automated global exploration for all reaction pathways on quantum chemical PES of a given chemical formula [32–34]. The most efficient way of quantum chemical samplings on PES can be made, if samplings are confined around reaction pathways. The numbers of equilibrium (EQ) and TS structures are finite, and their connections are also in the limited area along the reaction coordinates with essentially one-dimensional nature which can be described by small numbers of sampling points. Downhill walks from TS toward EQ or dissociation channel (DC) along reaction pathways on PES can easily be made by conventional methods, such as the steepest decent method or its modifications [23,28]. Whereas for uphill walks from EQ toward TS or DC along reaction pathways on PES, no algorithm has been reported before the anharmonic downward distortion (ADD) following proposed by the authors [32]. The common feature of reaction channels from an EQ point can be summarized as ADD, as indicated by arrows in Fig. 1. On going toward DC, the potential energy curve becomes flattened over the long distance. The presence of another EQ (EQ′) around an EQ leads to a saddle (TS). Such propensities due to the existence of another DC or EQ affect the local properties of potentials around an EQ. It follows that ADD around an EQ point can be considered as an indicator (or a compass) of the chemical reaction [32–34]. By noting ADD, a new method for finding reaction paths around EQ has been established as an uphill walking method for GRRM. The GRRM method based on the ADD-following has been applied to relatively small molecules [32–47]

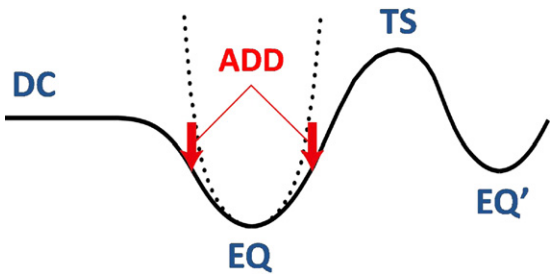

Fig. 1. Common features of potential energy curves for chemical reactions on going from an equilibrium structure (EQ) toward a dissociation channel (DC) or another equilibrium structure (EQ′) via a transition structure (TS). Anharmonic downward distortion (ADD, denoted by thick solid arrow) of the real potential from the harmonic potential (shown by dotted line) indicates the direction of the chemical reactions toward DC or TS.

including photochemical reactions [48,49], atomic and molecular clusters [50–55], organometallic catalytic reactions [29,56–59], and large systems [60].

The RuX_2–BINAP-catalyzed asymmetric hydrogenation of β-keto esters in alcoholic solvent is highly enantioselective and shows very high catalytic-activities [61,62], where BINAP is (2,2′-bis(diphenylphosphino)-1,1′-binaphthyl) and X-atoms are halogens such as Cl, Br, and I. In this reaction, protonation of the reactant esters is shown to be a key point to improve the catalytic-activity [5,63]. Fig. 2 shows the catalytic cycle [5]. In this cycle, the RuHCl compound is the actual catalyst, which is produced in a ligand exchange reaction ($RuCl_2$-BINAP + H_2 → RuHCl–BINAP + HCl). In the step (I), the reactant molecule is adsorbed on the catalyst to form the σ-type chelate complex 3. The protonation of 3 increases the electrophilicity of the carbonyl carbon, and converts the geometry from σ to π, and assists the hydride transfer from the metal to the carbonyl in the step (II). Then, detachment of the product 5 followed by a reaction of 6 with H_2 regenerates the catalyst 1.

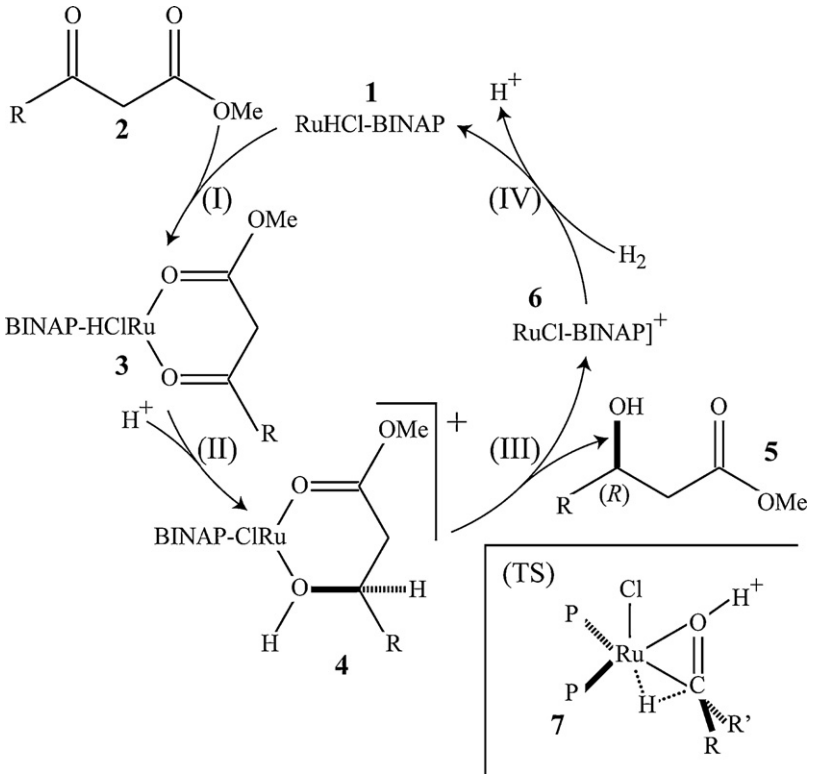

Fig. 2. The catalytic cycle and the chirality determining TS structure (inset).

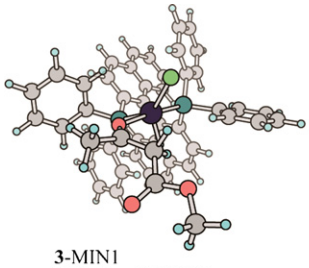

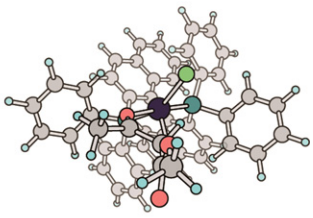

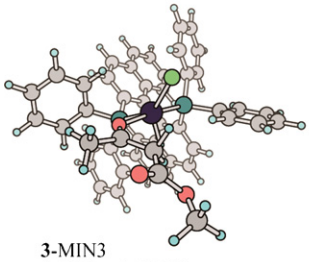

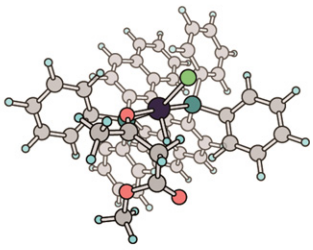

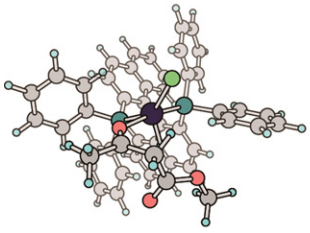

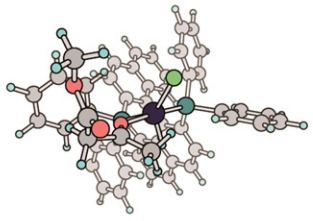

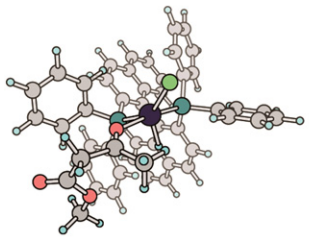

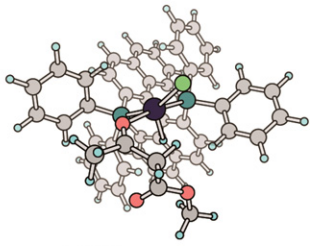

Fig. 3. The eight-lowest adsorption (local minimum) structures 3 (in terms of $\Delta G^{\#,0}$(373.15 K) from 3-MIN1) among 82 structures located in this study. Boltzmann distribution of each structure normalized in 3 are shown in parentheses.

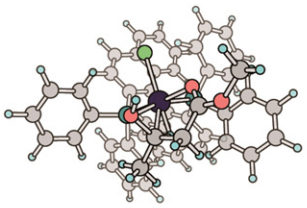

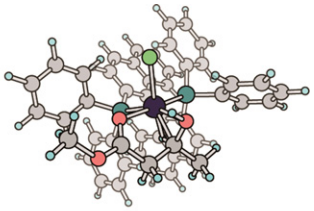

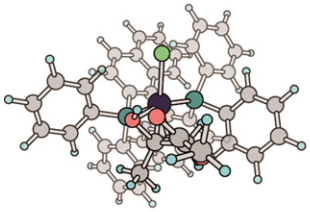

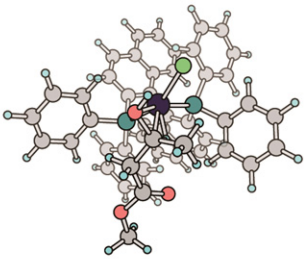

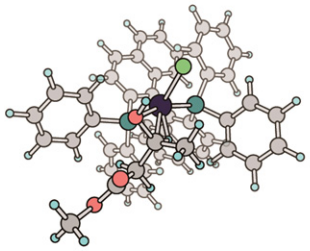

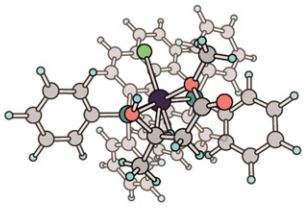

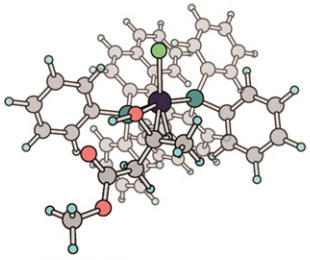

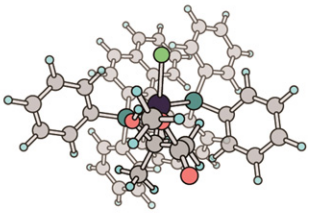

Fig. 4. The eight-lowest protonated TS structures 7 (in terms of $\Delta G^{\#,0}$(373.15 K) from 7-TS1) among 68 TSs located in this study. Boltzmann distribution of each structure normalized in 7 are shown in parentheses.

Table 1
Structural data for selected valence variables (see Scheme 1) and key distances δ_1 and δ_2 in 3-MIN1–8.[a].

	R_1	R_2	R_3	R_4	ϕ_1	ϕ_2	ϕ_3	ϕ_4	ϕ_5	δ_1[b]	δ_2[c]
3-MIN1	3.144	2.190	5.560	5.536	−5.8	−147.8	−166.0	−6.3	44.4	5.419	4.564
3-MIN2	3.135	2.184	5.690	5.660	−3.2	−172.9	−82.4	58.4	44.7	5.713	5.385
3-MIN3	3.154	2.189	5.815	5.470	−4.0	−174.1	153.5	−4.8	44.2	5.362	4.518
3-MIN4	3.106	2.176	4.293	4.280	−3.0	−80.4	−27.9	56.2	45.9	3.861	2.574
3-MIN5	3.154	2.193	4.178	3.944	5.5	−75.5	144.0	−3.4	43.1	3.382	2.692
3-MIN6	3.165	2.178	6.112	5.639	174.0	−117.7	99.0	−6.3	43.6	4.214	3.938
3-MIN7	3.178	2.186	5.916	4.718	−166.0	74.1	31.4	−6.1	47.6	3.397	2.640
3-MIN8	3.118	2.183	4.312	4.194	3.1	−84.0	152.4	44.5	46.0	3.663	2.619

[a] R and ϕ are in Å and degree, respectively.
[b] Distance in Å between a pair of the nearest heavy atoms in Ph groups in BINAP and $COOCH_3$ in the reactant.
[c] Distance in Å between a pair of the nearest atoms (including H) in Ph groups in BINAP and $COOCH_3$ in the reactant.

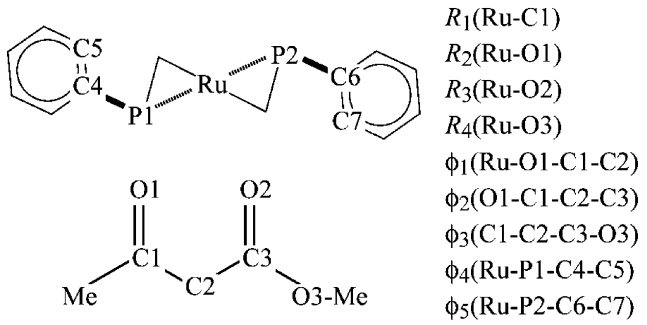

Scheme 1. Selected valence variables R_{1-4} and ϕ_{1-5}.

Here, 7 is the TS of the chirality determining step, which was systematically explored by the GRRM method in the previous study: a systematic search was made for conformers of 7 for the case that 2 is methyl-3-oxobutanoate (R = CH_3) [29]. In the present study, the entire reaction cycle of the same reaction was theoretically analyzed for both protonated and non-protonated systems.

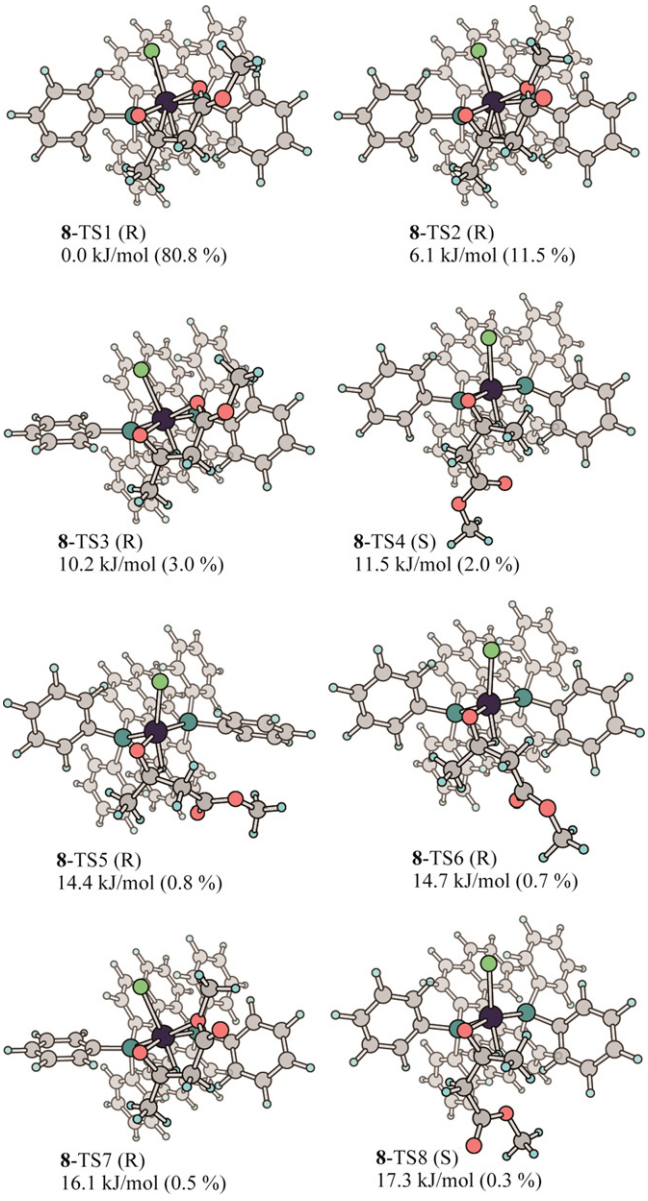

Fig. 5. The eight-lowest protonated TS structures 8 (in terms of $\Delta G^{\#,0}$(373.15 K) from 8-TS1) among 44 TSs located in this study. Boltzmann distribution of each structure normalized in 8 are shown in parentheses.

2. The GRRM method

2.1. Fundamental GRRM procedures

Since details of the GRRM method were reported in the previous papers [32–35], only outlines of the fundamental procedures are described here:

(1) At first, normal coordinates are determined at an EQ point.
(2) Around the EQ, PES is expanded in terms of scaled normal coordinates defined by $q_i = \lambda_i^{1/2} Q_i$, where Q_i is a normal coordinate with a respective eigenvalue λ_i.
(3) Reaction path points are determined as energy minima on a scaled hypersphere with a center at the EQ.
(4) Using several sizes of hypersphere, one can obtain series of points for the reaction pathways around the EQ.
(5) Indication of a TS region can be recognized from first order derivatives along the reaction path points. Location of each TS can be determined precisely by a conventional technique in the TS region [64,65].
(6) Asymptotic behavior separating a fragment from the remaining part indicates a DC.
(7) After arriving at TS, a conventional downhill technique, i.e., intrinsic reaction coordinate (IRC) technique [66–69], is used to reach an EQ or DC (or return to the current EQ). During this procedure, the IRC is determined (confirmed) from each TS toward both sides.
(8) Structures of newly found TS, DC, and EQ are compared with those of already found ones.
(9) After those procedures (1)–(8) starting from the current EQ are finished, normal coordinate calculations corresponding to the process (1) are performed for the next EQ. Then, subsequent processes from (2) to (8) are repeated around the new current EQ to discover successively TS, EQ, or DC. These cyclic procedures should be repeated for every new EQ, until no unprocessed EQ remains. All reaction channels via TS are confirmed as IRC during the above cyclic procedures.
(10) Entire reaction path connections are discovered one after another in a systematic way by the above procedures to yield a global reaction route map for a given chemical composition automatically (examples of such maps are found in Refs. [32–35,39,40,43–45].

2.2. Large ADD-following (l-ADDF)

The fundamental GRRM procedures include the full ADD-following (*f*-ADDF), which is rather too heavy when only the lower energy structures play key roles. Most chemical reactions in thermal conditions are the cases where low-barrier pathways are decisively important. Here, one may note the Bell–Evans–Polanyi (BEP) principle that a location of a TS leading to a lower energy EQ is much closer to the current EQ than that connected with the higher energy EQs [70,71].

Based on the BEP principle, a criterion can be introduced to reduce a number of ADDs to be followed that *L* largest ADDs are selected as important reaction paths leading to the lower energy EQs, because the larger stabilization interactions causing the lower energy EQ should have the larger influence around the current EQ to deform its harmonic potential downward. The efficiency of the ADD-following can be increased with the aid of the iterative optimization elimination (IOE) technique [33]. At the initial hypersphere, 3*L* ADDs are searched by the IOE technique. Among these,

Table 2
Structural data for selected valence variables (see Scheme 1) and key distances δ_1 and δ_2 in 7-TS1–8.[a].

	R_1	R_2	R_3	R_4	ϕ_1	ϕ_2	ϕ_3	ϕ_4	ϕ_5	δ_1[b]	δ_2[c]
7-TS1	2.149	2.231	2.240	4.256	106.5	−61.7	167.8	65.7	48.8	3.146	2.951
7-TS2	2.184	2.362	2.220	4.250	−106.7	61.1	−165.9	−37.9	55.6	3.038	2.854
7-TS3	2.185	2.208	4.130	5.241	101.7	36.8	145.5	67.9	43.2	4.857	4.857
7-TS4	2.262	2.255	4.065	5.116	−118.8	161.0	−174.1	69.7	36.4	3.354	2.531
7-TS5	2.270	2.248	4.995	5.493	−117.1	−65.4	166.0	69.1	36.1	4.302	4.290
7-TS6	2.149	2.224	4.325	2.308	107.7	−58.7	−8.0	65.8	47.5	3.317	2.600
7-TS7	2.183	2.189	4.436	5.572	−121.8	−38.4	−138.0	69.7	44.1	3.613	3.613
7-TS8	2.188	2.216	5.346	4.217	102.3	51.6	−62.3	68.1	43.6	4.842	4.842

[a] R and ϕ are in Å and degree, respectively.
[b] Distance in Å between a pair of the nearest heavy atoms in Ph groups in BINAP and $COOCH_3$ in the reactant.
[c] Distance in Å between a pair of the nearest atoms (including H) in Ph groups in BINAP and $COOCH_3$ in the reactant.

larger 2L are followed on the subsequent hyperspheres. When L reaction paths reach the neighboring potential well, the large ADD-following (l-ADDF) procedures are stopped. This l-ADDF technique [52] considerably reduces computational demands. After arriving at new potential wells, geometry optimizations are performed to obtain the structures of new EQs. During these procedures, TSs may also be determined if they are required. In this way, lower EQ and lower TS can be efficiently searched around an EQ point by the l-ADDF method.

2.3. Double-ended ADD-following (d-ADDF)

In the fundamental GRRM method, the ADD-following is processed with the expansion of hyperspheres. In the double-ended ADD-following (d-ADDF) method, the sphere contraction mode is employed to search intermediate structures very efficiently [38,50]. When a couple of EQs, EQa and EQb, are known, one can introduce a hypersphere so that EQa is located at the center and that EQb is on the surface. In this situation, the radius of the hypersphere is just the distance between EQa and EQb. When the size of the hypersphere is contracted keeping the center at the same position, important structures between EQa and EQb will be located on the minima of the hypersphere. This double-ended search is very efficient, because only one path is followed from the outside toward inside.

3. ONIOM–GRRM computations

All structures and energies were calculated in the ONIOM (B3LYP:UFF) framework, where all carbon and hydrogen atoms in BINAP were treated by UFF. In geometry optimization and harmonic vibrational analysis, the LANL2ZD basis with an extra set of f-functions [72] (LANL2DZ+f) was employed for Ru, and the 6-31G* set was used for others (BS1). Structure of 7 are taken from Ref. 29, where the 6-311++G** basis set was used for some important atoms directly involved in the hydride transfer reaction (BS1′). To illustrate the entire reaction profile based on the present (BS1) and previous (BS1′) geometries, single-point energy calculations were performed for all geometries using the LANL2DZ+f and 6-311++G** basis sets (BS2). All the energetics shown below are based on ONIOM (B3LYP/BS2:UFF) single-point energies. Zero-point-energy (ZPE) values were estimated by Harmonic vibrational analyses. Standard state free-energy of activation at 100 °C $\Delta G^{\#,0}$(373.15 K) were estimated assuming the Harmonic and rigid-rotor approximations for vibrational and rotational energy-levels, respectively, where the normal mode analysis was done with the basis set employed in the corresponding geometry optimization. Energy, gradient, and Hessian of the ONIOM method were computed by the Gaussian 03 programs [73], whereas all geometry movements were treated by the GRRM program [32–34].

4. Results and discussions

4.1. Adsorption structures

The adsorption structure 3 has three types: (1) the chelate σ-type complex, (2) the π-type complex, and (3) the single σ-type complex. Furthermore, there are numerous conformers of these three types. Therefore, structures of 3 were systematically explored by the GRRM/l-ADDF method [52]. Here, the initial automated search was done with a very small basis set, LANL2ZD for Ru, 6-31G* for P and Cl, and 6-31G for others, and all the obtained structures were reoptimized with the BS1. The search found 82 independent local minima, where all the 82 structures have the carbonyl oxygen coordination. Fig. 3 shows the eight-lowest structures in terms of $\Delta G^{\#,0}$(373.15 K) from 3-MIN1. Structural data for important valence variables (defined in Scheme 1) and interfragment distances between a Ph group in BINAP and $COOCH_3$ in the reactant in these structures are listed in Table 1. As seen in Fig. 3, all the lowest lying structures are the single σ-type without coordination of another oxygen atom. In spite of many chelate σ-type complexes in the database, the lowest chelate σ-type complex is the 44th lowest. The product chirality is determined at 3 if the chelate complex is very stable, because exchange of two coordination bonds in O–Ru–O is difficult in general. Fig. 3 shows Boltzmann distribution

Table 3
Structural data for selected valence variables (see Scheme 1) and key distances δ_1 and δ_2 in 8-TS1–8.[a].

	R_1	R_2	R_3	R_4	ϕ_1	ϕ_2	ϕ_3	ϕ_4	ϕ_5	δ_1[b]	δ_2[c]
8-TS1	2.265	2.131	2.223	4.249	99.6	−46.8	157.2	64.3	45.5	3.151	3.151
8-TS2	2.270	2.120	4.330	2.318	100.6	−37.3	−35.8	63.3	44.9	3.250	2.882
8-TS3	2.300	2.162	2.208	4.249	99.0	−45.7	156.4	62.2	−37.1	3.093	3.093
8-TS4	2.319	2.110	4.346	5.402	−117.7	165.7	177.4	62.5	44.2	3.456	2.629
8-TS5	2.333	2.105	4.093	4.687	103.9	−147.3	156.1	−29.6	49.6	3.552	3.076
8-TS6	2.362	2.103	4.348	5.400	107.8	−170.8	−166.2	60.0	43.8	3.492	2.620
8-TS7	2.307	2.149	4.335	2.302	100.1	−36.3	−35.6	61.3	−37.0	3.180	2.767
8-TS8	2.322	2.118	5.653	4.287	−120.1	−177.6	−47.3	61.1	44.6	3.378	2.498

[a] R and ϕ are in Å and degree, respectively.
[b] Distance in Å between a pair of the nearest heavy atoms in Ph groups in BINAP and $COOCH_3$ in the reactant.
[c] Distance in Å between a pair of the nearest atoms (including H) in Ph groups in BINAP and $COOCH_3$ in the reactant.

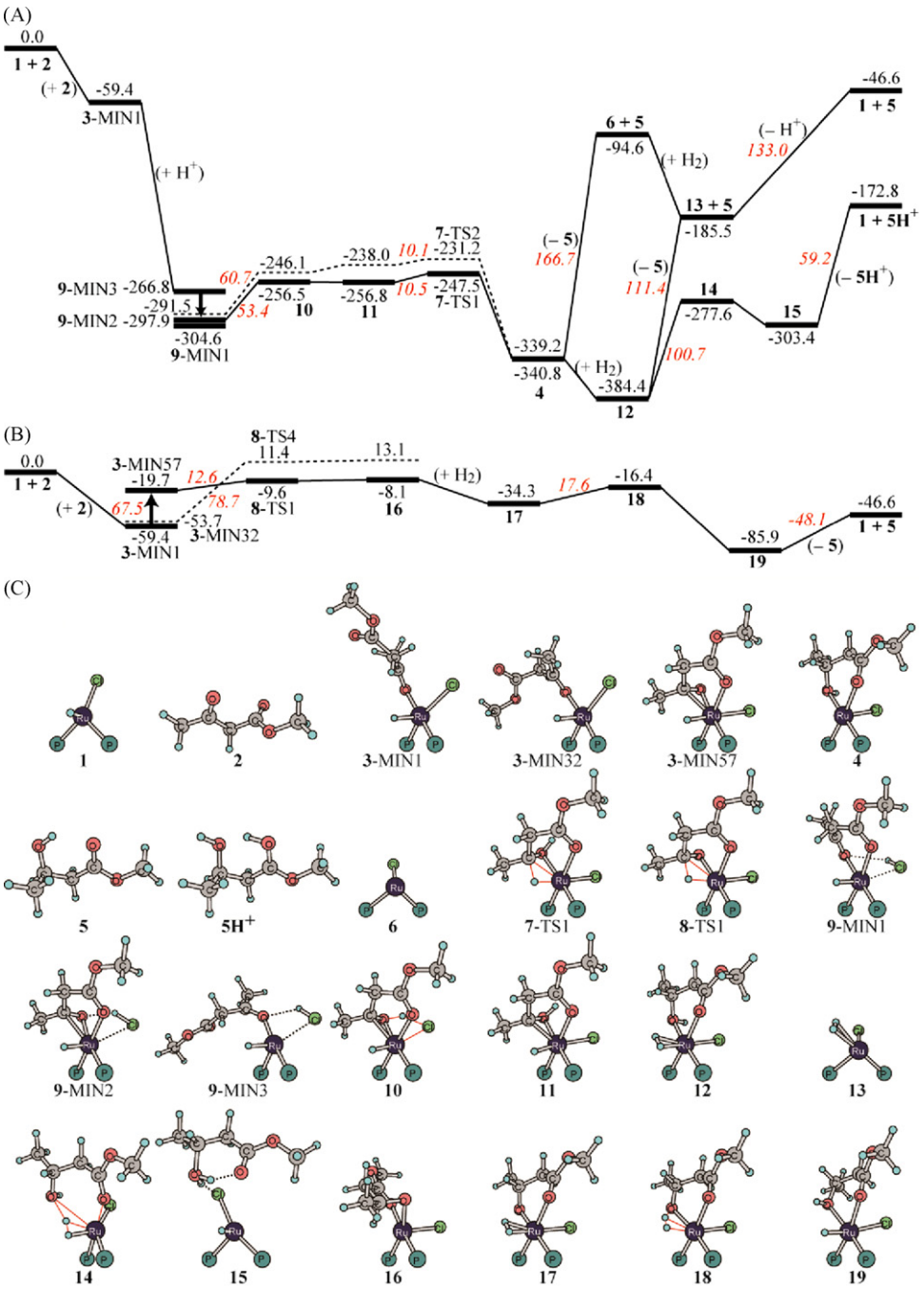

Fig. 6. Catalytic reaction cycles for (A) the protonated system and (B) the non-protonated system. Relative energy values shown in regular characters correspond to potential energy values including harmonic ZPE corrections (in kJ/mol), whereas $\Delta G^{\#,0}$(373.15 K) values are shown in (red) italic characters. Dashed lines show profiles leading to the minor product. In the protonated part, the (computed) proton affinity of CH_3OH (748.2 kJ/mol) is added assuming that the proton comes from the alcoholic solvents. Reaction center geometries for structures in (A) and (B) are listed in (C), where covalent and coordination bonds rearranging at TS structures are shown in (red) thin lines.

of each structure at 100 °C. Many conformers with different valence variables have non-negligible populations suggesting that the reactant molecule does not have a specific form at 3. It follows that the product chirality is not determined at 3. Among the 82 structures, the lowest π-type complex is very unstable as suggested previously [5], where its $\Delta G^{\#,0}$(373.15 K) from 3-MIN1 is 67.5 kJ/mol.

4.2. TS structures of the chirality determining step in the protonated system

The conformers for 7 were systematically searched by the GRRM/*l*-ADDF method [52]. Here, the structure of reaction center (P_2RuHCl–O=C) was fixed at an optimized TS structure, and UFF was used in the conformation sampling. All TS candidates were reoptimized to true TSs in full dimension at the ONIOM (B3LYP/BS1′:UFF) level. Fig. 4 lists the eight-lowest TS structures among 68 TSs in terms of $\Delta G^{\#,0}$(373.15 K) from 7-TS1[29]. Structural data for important valence variables (defined in Scheme 1) and interfragment distances between a Ph group in BINAP and $COOCH_3$ in the reactant in these structures are listed in Table 2. All of 68 TSs are for the hydride transfer reaction from the metal to the carbonyl. Here, structures with positive ϕ_1 value correspond to TSs leading to the product with the *R*-type chirality, whereas those for the *S*-type product have a negative ϕ_1 value. The low-

est 7-TS1 leads to the *R*-type product, while the lowest TS for the *S*-type (7-TS2) is 15.8 kJ mol^{-1} higher. A comparison between the lowest TSs for each product type clearly shows that the *R*-type is the main product in agreement with the experiment [61,62]. Boltzmann distribution shows that relative population of 7-TS1 vs. 7-TS2 is 164:1, which is also in line with the experimental enantio-excess value of >99%ee qualitatively. Although coordination manners in 7-TS1 and 7-TS2 are very similar, 7-TS1 is more stable than 7-TS2 because of the closer distance between one of phenyl groups in BINAP and the $COOCH_3$ group in 7-TS2, where the interfragment distances between the Ph and $COOCH_3$ groups in 7-TS1 and 7-TS2 are 2.951 and 2.854 Å, respectively. The shorter distance in 7-TS2 is caused by a restriction that the carbonyl group must coordinate along the Ru–H bond to take the hydride ligand from the Ru atom.

4.3. TS structures of the chirality determining step in the non-protonated system

A similar search was performed for the non-protonated TS 8. Fig. 5 shows the eight-lowest TS structures among 44 TSs in terms of $\Delta G^{\#,0}$(373.15 K) from 8-TS1. Structural data for important valence variables (defined in Scheme 1) and interfragment distances between a Ph group in BINAP and $COOCH_3$ in the reactant in these structures are listed in Table 3. All of the 44 TSs are for the metal-to-carbonyl hydride transfer reaction. The lowest 8-TS1 again leads to the *R*-type product, and the fourth lowest 8-TS4 was the lowest *S*-type TS with the 11.5 kJ mol^{-1} higher energy. The *R*-type is the main product also without the protonation. Boltzmann distribution shows that relative population of the *R*-type vs. the *S*-type is 42:1, which is rather worse than the computational value for the protonated system. One reason is the C–Ru distance at the TSs, which are 2.149, 2.184, 2.265, and 2.319 Å in 7-TS1, 7-TS2, 8-TS1, and 8-TS4, respectively. Elongation of the C–Ru distance weakens the steric interactions between the reactant molecule and BINAP, and consequently, lowers the selectivity. The longer C–Ru distances in 8-TS1 and 8-TS4 are due to the lower electrophilicity of the C atom in the non-protonated system. Although the lower electrophilicity affects on the catalytic-activity as suggested previously [5] and shown below, it has a significant effect also on the enantioselectivity.

4.4. Entire mechanism of the catalytic cycle

Finally, the entire catalytic cycles is shown in Fig. 6 for both (A) protonated and (B) non-protonated systems. Energy values shown in Fig. 6 are relative potential energy including the ZPE correction. Dashed lines show profiles leading to the minor *S*-type product. In the protonated part, the computed proton affinity (B3LYP/6-311++G**//6-31G*) of CH_3OH (748.2 kJ/mol) is added assuming that the proton comes from the alcoholic solvents. Reaction center geometries of the QM atoms for structures in (A) and (B) are listed in (C). In this search, TSs were located by the GRRM/*d*-ADDF method [38,50] for assumed connections in Fig. 2.

In both systems, the initial step is the reactant coordination, mainly generating 3-MIN1. The proton attached to the carbonyl oxygen in 3-MIN1 moves automatically (without any barrier) to the Cl ligand generating 9-MIN3 with an HCl moiety. A similar barrierless proton transfer occurs from the lowest chelate σ-type complex. Only a π-type complex can keep the proton at the carbonyl oxygen site in 11. Since 11 is just a metastable intermediate between 9 and 4, 11 likely collapses into 9 before going to 4. The reaction step from 9 to 4 can be regarded to be one step with overall $\Delta G^{\#,0}$(373.15 K) of 63.9 kJ/mol (7-TS1–9-MIN2) because of the very short life of 11. Here, this is the chirality determining step and the dashed line for the *S*-type product is always higher than the *R*-type.

Table 4
The five-lowest harmonic frequencies (in cm^{-1}) in 3-MIN1–8, 7-TS1–8, and 8-TS1–8.

	ω_1	ω_2	ω_3	ω_4	ω_5
3-MIN1	6.3	13.8	16.4	23.6	25.4
3-MIN2	8.2	13.1	18.6	22.0	35.0
3-MIN3	10.9	15.0	16.8	24.0	29.7
3-MIN4	7.5	13.7	28.8	29.3	38.3
3-MIN5	13.5	16.3	28.1	34.0	38.0
3-MIN6	9.1	12.7	15.9	23.3	28.3
3-MIN7	14.4	22.7	25.8	29.7	32.1
3-MIN8	9.0	27.9	29.7	34.5	37.3
7-TS1	−650.9	16.7	34.7	41.6	47.7
7-TS2	−611.8	16.8	33.8	43.2	44.8
7-TS3	−699.8	13.0	22.1	31.8	37.9
7-TS4	−487.8	19.6	26.7	33.9	42.5
7-TS5	−411.9	14.0	15.8	30.3	35.6
7-TS6	−613.4	19.6	34.5	41.8	42.8
7-TS7	−671.3	13.5	17.8	34.5	36.4
7-TS8	−699.5	14.1	28.5	32.7	35.2
8-TS1	−490.2	17.2	33.0	38.0	42.7
8-TS2	−462.2	19.3	36.1	41.4	43.6
8-TS3	−499.2	17.5	37.6	44.7	47.1
8-TS4	−469.9	15.3	21.1	34.2	38.1
8-TS5	−421.1	20.4	24.6	37.4	39.3
8-TS6	−521.1	12.2	23.6	34.9	38.9
8-TS7	−467.5	18.3	39.5	44.8	46.8
8-TS8	−481.4	10.5	19.4	35.4	37.1

Although the detachment of the product 5 is the next step in the proposed mechanism in Fig. 2, such a simple elimination requires very high energy of 166.7 kJ/mol (simultaneous adsorption of the solvent CH_3OH may lower the value). This barrier can be lowered to 111.4 kJ/mol if H_2 adsorption (4–12) occurs beforehand. The proton transfer from 13 to CH_3OH ($14+5 \rightarrow 1+5$) again requires a high energy of 133.0 kJ/mol. Here, an energetically better route is $12 \rightarrow 14 \rightarrow 15 \rightarrow 1+5H^+$ generating the catalyst 1 and protonated $5H^+$. This is because 5 has much higher proton affinity than CH_3OH, and consequently, the route to $5H^+$ is much more exothermic than the route to 5. The proton on 5 may be removed either in a long dynamics in solution or in the solvent evaporation step in experiments.

As discussed above, the π-type complexes are not very stable in the non-protonated system, where generation of the precursor of the hydride transfer 3-MIN57 requires at least $\Delta G^{\#,0}$(373.15 K) of 67.5 kJ/mol. Moreover, there is no π-type precursor for the *S*-type product because it is too unstable to form a local minimum on the PES. Furthermore, the product of the hydride transfer 16 is just a metastable structure which can immediately go back to 3 before the H_2 coordination in the next step. It follows that the unstable 16 is another reason of the low catalytic-activity in the non-protonated system. The H_2 cleavage process at 18 is not very difficult with $\Delta G^{\#,0}$(373.15 K) of 17.6 kJ/mol if 16 exists with sufficient amount. Total exothermicity of the non-protonated cycle is only 46.6 kJ/mol. Three reasons for the low catalytic-activity in the non-protonated system can thus be suggested: (1) the unstable π-type complex 3-MIN57, (2) the metastable hydride transfer product 16, and (3) the low exothermicity in the non-protonated system.

In this study, the harmonic approximation was employed to estimate the ZPE and $\Delta G^{\#,0}$(373.15 K) values. Some errors may be involved because of very low harmonic frequencies as shown in Table 4. The errors can be assumed to be vanishing in the relative energies among similar structures in Fig. 4. Especially, the key structures (7-TS1 and 7-TS2) have very close frequencies. Hence, the low frequency issue is not very important in the discussions on selectivity in Fig. 4, whereas the energy profile in Fig. 6 might change because of different frequencies in structures of different steps. There is another problem to use $\Delta G^{\#,0}$(373.15 K) for bimolecular (AB → A + B) reactions (i.e., $4 \rightarrow 6+5$, $12 \rightarrow 13+5$, and $15 \rightarrow 1+5H^+$ in Fig. 6), because $\Delta G^{\#,0}$(373.15 K) is assuming the standard

state. Hence, the latter half of the profile (i.e., after the chirality determining step) may change depending on the experimental concentration. Another important factor which was not taken into account is solvation effects. Although it can change the profile significantly, it is also not very important for discussions on selectivity (i.e., relative energy of 7-TS1 and 7-TS2), because its effects can be negligible due to the similar chemical interactions in the two structures with only a slight difference in the steric repulsion.

5. Concluding remarks and perspectives

An automated exploration of reaction channels on potential energy surfaces has become possible by the GRRM method, in which the anharmonic downward distortion (ADD) of the potential indicates the direction of the chemical reaction route. ADD can be used as a 'compass' to discover unknown chemistry [32–35]. Associated techniques of the GRRM method, *l*-ADDF [52] and *d*-ADDF [38,50], have made it possible to elucidate catalytic reaction mechanisms for large systems, such as a Ru-BINAP complex for asymmetric hydrogenation.

In the present application to a RuHCl–BINAP-catalyzed asymmetric hydrogenation reaction, its high enantioselectivity was explained by comparing the stability of TS structures for each optical isomer obtained by an extensive sampling of their conformers. Entire reaction profiles were illustrated for the catalytic cycles with and without protonation. Four kinds of effects of the protonation were discussed: (1) the shortening of the C–Ru distance in the chirality determining TS to improve enantioselectivity, (2) the increased stability of π-type adsorption complexes, (3) the stabilization of the hydride transfer reaction products, and (4) the enhancement of the exothermicity of the catalytic cycle.

We performed three types of analyses to elucidate the full reaction mechanism of the RuHCl-catalyzed asymmetric hydrogenation: (1) the adsorption structure sampling by the GRRM/*l*-ADDF method [52], (2) the conformation sampling at the chirality determining TS by the GRRM/*l*-ADDF method [52], and (3) the reaction path search by the GRRM/*d*-ADDF method [38,50]. These calculations as a whole are expected to yield a full reaction mechanism as shown above. Although the third step requires guesses of connections in the *d*-ADDF calculations, this step will also be automated by using the microiteration-ADD-following (μ-ADDF) method which was developed very recently by a combination of the microiteration technique [74,75] and the ADD-following method [60]. The present approach based on the GRRM method is promising to explore unknown mechanisms of asymmetric hydrogenation reactions.

Acknowledgements

K.O. acknowledges the Grants-in-Aid for Scientific Research (Nos. 21350007 and 21655002) from the Ministry of Education, Science, Sports, and Culture. S.M. is supported by a Research Fellowship of Japan Society of Promotion of Science for Young Scientists.

References

[1] R. Noyori, Asymmetric Catalysis in Organic Synthesis, Wiley, New York, 1994.
[2] W.S. Knowles, Angew. Chem., Int. Ed. 41 (2002) 1998.
[3] R. Noyori, Angew. Chem., Int. Ed. 41 (2002) 2008.
[4] H.-U. Blaser, B. Pugin, F. Spindler, J. Mol. Catal. A: Chem. 231 (2005) 1.
[5] R. Noyori, M. Kitamura, T. Ohkuma, Proc. Natl. Acad. Sci. U.S.A. 101 (2004) 5356.
[6] D.G. Musaev, K. Morokuma, Adv. Chem. Phys. 95 (1996) 61.
[7] T. Ziegler, J. Autschbach, Chem. Rev. 105 (2005) 2695.
[8] D. Balcells, F. Maseras, New J. Chem. 31 (2007) 333.
[9] K.N. Houk, P.H.-Y. Cheong, Nature 455 (2008) 309.
[10] J.M. Brown, R.J. Deeth, Angew. Chem., Int. Ed. 48 (2009) 4476.
[11] N. Fey, Dalton Trans. 39 (2010) 296.
[12] A.D. Becke, J. Chem. Phys. 98 (1993) 5648.
[13] Y. Zhao, D.G. Truhlar, Acc. Chem. Res. 41 (2008) 157.
[14] J.J.P. Stewart, J. Mol. Model 13 (2007) 1173.
[15] G. Zheng, H. Witek, P. Bobadova-Parvanova, S. Irle, D.G. Musaev, R. Prabhakar, K. Morokuma, M. Lundberg, M. Elstner, C. Köhler, T. Frauenheim, J. Chem. Theory Comput. 3 (2007) 1349.
[16] P. Rydberg, L. Olsen, P.-O. Norrby, U. Ryde, J. Chem. Theory Comput. 3 (2007) 1765.
[17] A. Warshel, M. Levitt, J. Mol. Biol. 103 (1976) 227.
[18] U.C. Singh, P.A. Kollman, J. Comput. Chem. 7 (1986) 718.
[19] M.J. Field, P.A. Bash, M. Karplus, J. Comput. Chem. 11 (1990) 700.
[20] F. Maseras, K. Morokuma, J. Comput. Chem. 16 (1995) 1170.
[21] M. Svensson, S. Humbel, R.D.J. Froese, T. Matsubara, S. Sieber, K. Morokuma, J. Phys. Chem. 100 (1996) 19357.
[22] K. Morokuma, Bull. Korean Chem. Soc. 24 (2003) 797.
[23] H.B. Schlegel, J. Comp. Chem. 24 (2003) 1514.
[24] C.R. Landis, S. Feldgus, Angew. Chem., Int. Ed. 39 (2000) 2863.
[25] S. Feldgus, C.R. Landis, J. Am. Chem. Soc. 112 (2000) 12714.
[26] I.D. Gridnev, T. Imamoto, Acc. Chem. Res. 37 (2004) 633.
[27] S. Mori, T. Vreven, K. Morokuma, Chem. Asian J. 1 (2006) 391.
[28] F. Jensen, Introduction to Computational Chemistry, 2nd ed., Wiley, Chichester, 2007.
[29] S. Maeda, K. Ohno, J. Am. Chem. Soc. 130 (2008) 17228.
[30] P.J. Donoghue, P. Helquist, P.-O. Norrby, O. Wiest, J. Am. Chem. Soc. 131 (2009) 410.
[31] P.J. Donoghue, P. Helquist, P.-O. Norrby, O. Wiest, O.J. Chem, Theory Comput. 4 (2008) 1313.
[32] K. Ohno, S. Maeda, Chem. Phys. Lett. 384 (2004) 277.
[33] S. Maeda, K. Ohno, J. Phys. Chem. A 109 (2005) 5742.
[34] K. Ohno, S. Maeda, J. Phys. Chem. A 110 (2006) 8933.
[35] K. Ohno, S. Maeda, Phys. Scripta 78 (2008) 058122.
[36] S. Maeda, K. Ohno, Chem. Lett. 33 (2004) 1372.
[37] S. Maeda, K. Ohno, Chem. Phys. Lett. 398 (2004) 240.
[38] S. Maeda, K. Ohno, Chem. Phys. Lett. 404 (2005) 95.
[39] X. Yang, S. Maeda, K. Ohno, J. Phys. Chem. A 109 (2005) 7319.
[40] X. Yang, S. Maeda, K. Ohno, Chem. Phys. Lett. 418 (2006) 208.
[41] S. Maeda, K. Ohno, Astrophys. J. 640 (2006) 823.
[42] K. Ohno, S. Maeda, Chem. Lett. 35 (2006) 492.
[43] X. Yang, S. Maeda, K. Ohno, J. Phys. Chem. A 111 (2007) 5099.
[44] Y. Watanabe, S. Maeda, K. Ohno, Chem. Phys. Lett. 447 (2007) 21.
[45] S. Maeda, K. Ohno, Chem. Phys. Lett. 460 (2008) 55.
[46] Y. Luo, S. Maeda, K. Ohno, Chem. Phys. Lett. 469 (2009) 57.
[47] M. Moteki, S. Maeda, K. Ohno, Organometallics 28 (2009) 2218.
[48] S. Maeda, K. Ohno, K. Morokuma, J. Phys. Chem. A 113 (2009) 1704.
[49] P. Zhang, S. Maeda, K. Morokuma, B.J. Braams, J. Chem. Phys. 130 (2009) 114304.
[50] S. Maeda, K. Ohno, J. Chem. Phys. 124 (2006) 174306.
[51] B. Hajgató, S. Maeda, K. Ohno, AIP Conf. Proc. 855 (2006) 296.
[52] S. Maeda, K. Ohno, J. Phys. Chem. A 111 (2007) 4527.
[53] Y. Luo, S. Maeda, K. Ohno, J. Phys. Chem. A 111 (2007) 10732.
[54] S. Maeda, K. Ohno, J. Phys. Chem. A 112 (2008) 2962.
[55] Y. Luo, S. Maeda, K. Ohno, J. Comput. Chem. 30 (2009) 952.
[56] S. Maeda, K. Ohno, J. Phys. Chem. A 111 (2007) 13168.
[57] Y. Luo, K. Ohno, Organometallics 26 (2007) 3597.
[58] Y. Luo, S. Maeda, K. Ohno, J. Phys. Chem. A 112 (2008) 5720.
[59] Y. Luo, S. Maeda, K. Ohno, Tetrahedron Lett. 49 (2008) 6841.
[60] S. Maeda, K. Ohno, K. Morokuma, J. Chem. Theory Comput. 5 (2009) 2734.
[61] M. Kitamura, M. Tokunaga, T. Ohkuma, R. Noyori, Org. Synth. Collect. 9 (1998) 589.
[62] M. Kitamura, M. Tokunaga, T. Ohkuma, R. Noyori, Org. Synth. 71 (1993) 1.
[63] M. Kitamura, M. Yoshimura, N. Kanda, R. Noyori, Tetrahedron 55 (1999) 8769.
[64] A. Banerjee, N. Adams, J. Simons, R. Shepard, J. Phys. Chem. 89 (1985) 52.
[65] Ö. Farkas, H.B. Schlegel, J. Chem. Phys. 111 (1999) 10806.
[66] K. Fukui, Acc. Chem. Res. 14 (1981) 363.
[67] K. Ishida, K. Morokuma, A. Komornicki, J. Chem. Phys. 66 (1977) 2153.
[68] M. Page, J.W. McIver Jr., J. Chem. Phys. 88 (1988) 922.
[69] C. Gonzalez, H.B. Schlegel, J. Chem. Phys. 90 (1989) 2154.
[70] R.P. Bell, Proc. R. Soc. Lond. Ser. A 154 (1936) 414.
[71] M.G. Evans, M. Polanyi, Trans. Faraday Soc. 32 (1936) 1333.
[72] A. Hollwarth, M. Bohme, S. Dapprich, A.W. Ehlers, A. Gobbi, V. Jonas, K.F. Kohler, R. Veldkamp, G. Frenking, Chem. Phys. Lett. 208 (1993) 111.
[73] M.J. Frisch, G.W. Trucks, H.B. Schlegel, G.E. Scuseria, M.A. Robb, J.R. Cheeseman, J.A. Montgomery Jr., T. Vreven, K.N. Kudin, J.C. Burant, J.M. Millam, S.S. Iyengar, J. Tomasi, V. Barone, B. Mennucci, M. Cossi, G. Scalmani, N. Rega, G.A. Petersson, H. Nakatsuji, M. Hada, M. Ehara, K. Toyota, R. Fukuda, J. Hasegawa, M. Ishida, T. Nakajima, Y. Honda, O. Kitao, H. Nakai, M. Klene, X. Li, J.E. Knox, H.P. Hratchian, J.B. Cross, C. Adamo, J. Jaramillo, R. Gomperts, R.E. Stratmann, O. Yazyev, A.J. Austin, R. Cammi, C. Pomelli, J.W. Ochterski, P.Y. Ayala, K. Morokuma, G.A. Voth, P. Salvador, J.J. Dannenberg, V.G. Zakrzewski, S. Dapprich, A.D. Daniels, M.C. Strain, O. Farkas, D.K. Malick, A.D. Rabuck, K. Raghavachari, J.B. Foresman, J.V. Ortiz, Q. Cui, A.G. Baboul, S. Clifford, J. Cioslowski, B.B. Stefanov, G. Liu, A. Liashenko, P. Piskorz, I. Komaromi, R.L. Martin, D.J. Fox, T. Keith, M.A. Al-Laham, C.Y. Peng, A. Nanayakkara, M. Challacombe, P.M.W. Gill, B. Johnson, W. Chen, M.W. Wong, C. Gonzalez, J.A. Pople, GAUSSIAN 03, Revision C.02, Gaussian, Inc., Wallingford, CT, 2004.
[74] T. Vreven, K. Morokuma, Ö. Farkas, H.B. Schlegel, M.J. Frisch, J. Comput. Chem. 24 (2003) 760.
[75] T. Vreven, M.J. Frisch, K.N. Kudin, H.B. Schlegel, K. Morokuma, Mol. Phys. 104 (2006) 701.